

# Research Articles



# Aqueous Batteri<u>es</u>

How to cite: *Angew. Chem. Int. Ed.* **2021**, *60*, 4169–4174 International Edition: doi.org/10.1002/anie.202011588 German Edition: doi.org/10.1002/ange.202011588

# **Boosting the Energy Density of Aqueous Batteries via Facile Grotthuss Proton Transport**

Qinghe Zhao<sup>+</sup>, Aoye Song<sup>+</sup>, Wenguang Zhao<sup>+</sup>, Runzhi Qin, Shouxiang Ding, Xin Chen, Yongli Song, Luyi Yang, Hai Lin, Shunning Li,\* and Feng Pan\*

Abstract: The recent developments in rechargeable aqueous batteries have witnessed a burgeoning interest in the mechanism of proton transport in the cathode materials. Herein, for the first time, we report the Grotthuss proton transport mechanism in  $\alpha$ -MnO<sub>2</sub> which features wide [2 × 2] tunnels. Exemplified by the substitution doping of Ni ( $\approx 5$  at.%) in  $\alpha$ - $MnO_2$  that increases the energy density of the electrode by  $\approx$  25%, we reveal a close link between the tetragonalorthorhombic (TO) distortion of the lattice and the diffusion kinetics of protons in the tunnels. Experimental and theoretical results verify that Ni dopants can exacerbate the TO distortion during discharge, thereby facilitating the hydrogen bond formation in bulk  $\alpha$ -MnO<sub>2</sub>. The isolated direct hopping mode of proton transport is switched to a facile concerted mode, which involves the formation and concomitant cleavage of O-H bonds in a proton array, namely via Grotthuss proton transport mechanism. Our study provides important insight towards the understanding of proton transport in MnO<sub>2</sub> and can serve as a model for the compositional design of cathode materials for rechargeable aqueous batteries.

## Introduction

Despite the spectacular success of lithium ion batteries (LIBs) over the past few decades for small-scale applications, <sup>[1]</sup> the safety issues arising from the flammable organic electrolytes, as well as the high price of Li, Co and Ni elements, have restrained their deployment in large-scale energy storage, such as grid energy storage systems and renewable energy sources. <sup>[2]</sup> Indeed, studies on alternative battery technologies are steadily increasing in recent years, among which the rechargeable aqueous batteries hold particular practicability due to their low flammability, high natural abundance, and good environment compatibility. <sup>[3]</sup> Intensive efforts have been directed towards the Zn-MnO<sub>2</sub> systems. <sup>[4]</sup> However, the industrialization of reversible aque-

ous Zn/MnO<sub>2</sub> cells is plagued by their insufficient energy density, mainly on account of the limited operating voltage, which is inherently suppressed by the narrow electrochemical stability window (ESW) of water. While the ESW can be expanded by the tailor design of electrolytes including "water-in-salt" electrolytes<sup>[5]</sup> and hydrate-melt electrolytes,<sup>[6]</sup> another intuitive approach to increase energy density is to improve the cathode capacity. Hence, there is a great need to elucidate the intercalation mechanisms of cations in the MnO<sub>2</sub> cathode, which can help to develop strategies for achieving high capacity delivery over a satisfactory life span.

Several studies have shown that when mild aqueous Znsalt electrolytes are employed, protons will inevitably participate in the electrochemical reaction as the charge carriers in Zn/MnO<sub>2</sub> cells. This is known as H<sup>+</sup>/Zn<sup>2+</sup> co-intercalation, which was first introduced by Wang's group in 2017.<sup>[7]</sup> Since then, the H<sup>+</sup>/Zn<sup>2+</sup> co-intercalation has been shown to prevail in MnO<sub>2</sub> cathodes regardless of the polymorphs, for example, tunnel-type  $\alpha$ -MnO<sub>2</sub><sup>[8]</sup> and  $\beta$ -MnO<sub>2</sub>, and layer-type  $\delta$ - $MnO_{2}$ , [10] etc. The ratio between intercalated H<sup>+</sup> and  $Zn^{2+}$  can vary among different polymorphs owing to the diversity of diffusion paths, such as the wide  $[2 \times 2]$  tunnels featured in  $\alpha$ - $MnO_2^{[11]}$  and the compact  $[1 \times 1]$  tunnels in  $\beta$ - $MnO_2^{[12]}$ Nevertheless, in general, promotion of  $H^+\!/Zn^{2+}$  co-intercalation presents a significant advance in the electrochemical performance of the corresponding cathode, with merits of higher capacity, [10a] better cyclability, [9] and superior rate capability.[10b] Accordingly, the detailed knowledge of proton transport mechanism in MnO<sub>2</sub> is a prerequisite for the development of high-performance aqueous batteries.

In this work, α-MnO<sub>2</sub> with Ni-doping is successfully synthesized, in which the tetragonal-orthorhombic (TO) distortion of the lattice is promoted by the Ni dopants during discharge, resulting in much higher capacity (increased by  $\approx 29\%$ , and close to the capacity limit), energy density (increased by  $\approx 25\%$ ) and power density (increased by  $\approx$  67%) as compared to the counterpart without doping. Based on the experimental and density functional theory (DFT) calculation results, we ascribe the improvement in electrochemical performance to a facilitating effect of TO distortion on Grotthuss proton transport. The Grotthuss mechanism of proton diffusion was postulated to describe the fast conduction of protons in aqueous mediates, and was recently interpreted as being attributable to the high-rate behavior of Turnbull's blue analogue electrodes that hosts abundant lattice water.<sup>[13]</sup> In this mechanism, protons are translocated through proton relay, which is accomplished via the concerted cleavage and formation of hydrogen-bonding

School of Advanced Materials, Peking University Shenzhen Graduate School

Shenzhen 518055 (P. R. China) E-mail: lisn@pku.edu.cn

panfeng@pkusz.edu.cn

[\*] These authors contributed equally to this work.

Supporting information and the ORCID identification number(s) for

the author(s) of this article can be found under: https://doi.org/10.1002/anie.202011588.

4169

<sup>[\*]</sup> Q. Zhao,<sup>[+]</sup> A. Song,<sup>[+]</sup> W. Zhao,<sup>[+]</sup> R. Qin, S. Ding, X. Chen, Y. Song, L. Yang, H. Lin, S. Li, Prof. F. Pan

5213773, 2021, 8, Downloaded from https://onlinelibrary.wiley.com/doi/10.1002/anie.202011588 by University Town Of Shenzhen, Wiley Online Library on [24/11/2025]. See the Terms and Conditions (https://onlinelbrary.wiley.com/terms-and-conditions) on Wiley Online Library of rules of use; OA articles are governed by the applicable Creative Commons. Licensea

among neighboring water molecules, presenting a scenario similar to Newton's cradle. [14] Here, as the first example, we demonstrate that the Grotthuss mechanism is also applicable to proton hopping on tunnel walls of solid-state materials. The comprehensive picture of cooperative proton transport in  $\alpha$ -MnO<sub>2</sub>, along with its modulation by the degree of TO distortion, can help us to capture the proton intercalation mechanism in other electrodes, and at the same time engender new opportunities for boosting the energy density of rechargeable aqueous batteries.

#### Results and Discussion

α-MnO<sub>2</sub> is composed of MnO<sub>6</sub> structural units, which are interlinked into chains via edge-sharing and are further assembled into one-dimensional tunnel framework via corner-sharing (Figure 1A). There are two kinds of tunnel sizes,  $[2 \times 2]$  and  $[1 \times 1]$ , both available for H<sup>+</sup> intercalation. The pre-intercalated  $K^+$  ions can reside in the  $[2 \times 2]$  tunnels and help to stabilize the structure. [15] We synthesized Ni-doped  $\alpha$ -MnO<sub>2</sub> via a simple one-step hydrothermal reaction using KMnO<sub>4</sub>, carbon black, and Ni(NO<sub>3</sub>)<sub>2</sub> as reactants. It is found that a layered polymorph of MnO<sub>2</sub> will emerge as a reaction product for  $Ni(NO_3)_2$  concentrations  $(C_{Ni(NO_3)_2})$  larger than  $0.2 \text{ mol L}^{-1}$  (Figure S1), and that higher  $C_{Ni(NO_3)_2}$  tends to result in more promising electrochemical performance (Figure S2). Accordingly, here we select the sample prepared with  $C_{Ni(NO_3)_2} = 0.2 \text{ mol L}^{-1}$  as the model compound for the study of Ni-doped α-MnO<sub>2</sub>. To identify the dopant location of Ni, Xray diffraction (XRD) refinements are conducted (Figure 1B

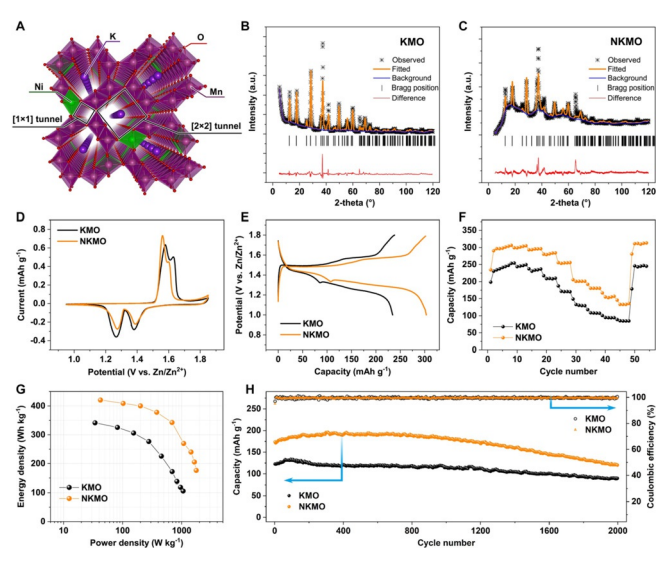


**Figure 1.** Structural characterization and electrochemical performance of KMO and NKMO electrodes. A) Ni-doped  $\alpha$ -MnO<sub>2</sub> with pre-intercalated K ions. (B and C) XRD refinement of the samples prepared with B)  $e_{Ni(NO_3)_2} = 0$  mol L<sup>-1</sup> (KMO) and C)  $e_{Ni(NO_3)_2} = 0.2$  mol L<sup>-1</sup> (NKMO). D) CV curves in potential range of 0.95–1.95 V with scan rate of 0.1 mV s<sup>-1</sup>. E) Galvanostatic charge/discharge curves at current of 0.05 C (1 C = 308 mAh g<sup>-1</sup>). F) Rate performances in the current range from 0.1 C to 10 C. G) Energy density and power density of KMO and NKMO electrodes. H) Long-term cycling performances and corresponding Coulombic efficiencies at current density of 4 C.

and C), which suggest that  $\approx\!5\,\%$  of the Mn sites are substituted by Ni. According to the results from inductively coupled plasma (ICP) and thermal-gravimetric analysis (TGA, Figure S3), the stoichiometry of the representative Ni-doped  $\alpha\text{-MnO}_2$  is determined as Ni\_0.052 K\_0.119 Mn\_0.948 O\_2-0.208 H\_2O (NKMO), whereas the reference sample prepared without Ni(NO\_3)2 is K\_0.112 MnO\_2·0.136 H\_2O (KMO). Scanning transmission electron microscope (STEM) results identify a small difference in lattice plane spacing between both samples (Figure S4), and reveal a uniform distribution of Ni in NKMO (Figure S5). The BET measurements (Figure S6) indicate that Ni-doping can increase the surface area, thus allowing more electrolyte to infiltrate into the cathode and leading to shortened ion diffusion distance.

The electrochemical performance of α-MnO<sub>2</sub> cathodes (electrode preparation is given in the Supporting Information) are investigated in coin cells using Zn plate as anode in 3 M ZnSO<sub>4</sub> + 0.2 M MnSO<sub>4</sub> aqueous electrolyte. Adding MnSO<sub>4</sub> in electrolyte is crucial for suppressing Mn<sup>2+</sup> dissolution<sup>[16]</sup> and promoting the capacity delivery of MnO<sub>2</sub> electrodes (Figure S7). We note that the capacity contribution from MnO<sub>2</sub>/Mn<sup>2+</sup> redox is negligible (< 0.2 %) during cycling (Figure S8). Cyclic voltammetry (CV) curves of Zn/KMO and Zn/NKMO cells are shown in Figure 1D and S9, in which two pairs of cathodic/anodic peaks correspond to H<sup>+</sup>/Zn<sup>2+</sup> insertion/extraction processes in KMO and NKMO electrodes, respectively. As compared with Zn/KMO, the Zn/NKMO cell shifts the cathodic peaks ( $\approx 1.26$  and  $\approx 1.38$  V) to higher values, and the anodic peaks ( $\approx 1.58$  and  $\approx 1.63$  V) to lower values. Combined with the observation of a narrower halfwidth of the anodic peaks for NKMO ( $\approx$  64 mV) than KMO ( $\approx$ 106 mV), it is clear that Ni-doping can induce depolarization in the cathode, which is potentially linked to a major change in diffusion kinetics of the ionic charge carriers. Figure 1E shows the galvanostatic charge/discharge curves of Zn/KMO and Zn/NKMO cells at current of 0.05C (active loading:  $> 1.5 \text{ mg cm}^{-2}$ ). The discharge capacity of Zn/ NKMO cell ( $\approx 303 \text{ mAh g}^{-1}$ ) is about 29% higher than that of Zn/KMO ( $\approx$  235 mAh g<sup>-1</sup>), which is surprising in view of the relatively low concentration of Ni in NKMO. The advantage of NKMO cathode in capacity delivery is well maintained even at high rates, as shown in Figure 1F and S10. A high energy density of 421 Whkg<sup>-1</sup> (at 0.1 C) and a maximum power density of 1766 Wkg<sup>-1</sup> (at 10 C) based on the active mass are displayed for NKMO (Figure 1G), which ranks it among the best reported MnO<sub>2</sub>-based cathodes for Zn-ion batteries (Table S1). The long-term cycling stability of Zn/KMO and Zn/NKMO cells examined at 4C (1C= 0.308 mAh mg<sup>-1</sup>, Figure 1 H) indicates that the above features of NKMO will require a slight sacrifice of capacity retention (73.6% for KMO vs. 71.4% for NKMO after 2000 cycles). This may be attributed to the enlarged surface area upon Ni doping that renders the electrode more susceptible to Mn<sup>2+</sup> dissolution.

To understand the doping effects, a detailed analysis of the ion intercalation mechanism from both experimental and theoretical aspects is carried out. Previous report by our group<sup>[9]</sup> has unraveled a ubiquitous  $H^+/Zn^{2+}$  synergistic intercalation in manganese oxide cathodes, which can be

assessed by comparing the capacities of cells with different electrolytes: only Zn<sup>2+</sup> and H<sup>+</sup> alone are intercalated into the cathode when using ZnSO<sub>4</sub>/dimethyl sulfoxide (DMSO) and MnSO<sub>4</sub>/H<sub>2</sub>O electrolytes, respectively, while H<sup>+</sup>/Zn<sup>2+</sup> cointercalation takes place with ZnSO<sub>4</sub>+MnSO<sub>4</sub>/H<sub>2</sub>O. Figure 2 A and S11 demonstrate that Ni doping can induce higher capacity for single  $Zn^{2+}$  (55.8 mAh g<sup>-1</sup>), single H<sup>+</sup>  $(141.6 \text{ mAh g}^{-1})$  and H<sup>+</sup>/Zn<sup>2+</sup>  $(299.4 \text{ mAh g}^{-1})$  intercalation than the KMO counterpart (54.8, 91.5, and 230.8 mAh g<sup>-1</sup>, respectively). It is noteworthy that for both electrodes, H<sup>+</sup>/ Zn<sup>2+</sup> co-intercalation yields extra capacity to the sum of single Zn<sup>2+</sup> and single H<sup>+</sup> intercalation, suggesting a synchronous (mutual promoting) effect of H<sup>+</sup> and Zn<sup>2+</sup> intercalation. The ICP results indicate that in the case of H<sup>+</sup>/Zn<sup>2+</sup> co-intercalation, Zn<sup>2+</sup> contributes to a capacity of 27.3 and 28.1 mAh g<sup>-1</sup> for KMO and NKMO, respectively. Thus, H+ intercalation dominates the capacity delivery in the co-intercalation process, whereas Zn<sup>2+</sup> intercalation, although non-negligible, is rather limited and may hardly be influenced by Ni doping, probably due to the sluggish diffusion kinetics of  $Zn^{2+}$  in  $\alpha$ -MnO<sub>2</sub> cathodes.

The intercalation mechanism is also unveiled by X-ray photoelectron spectroscopy (XPS), as shown in Figure 2B

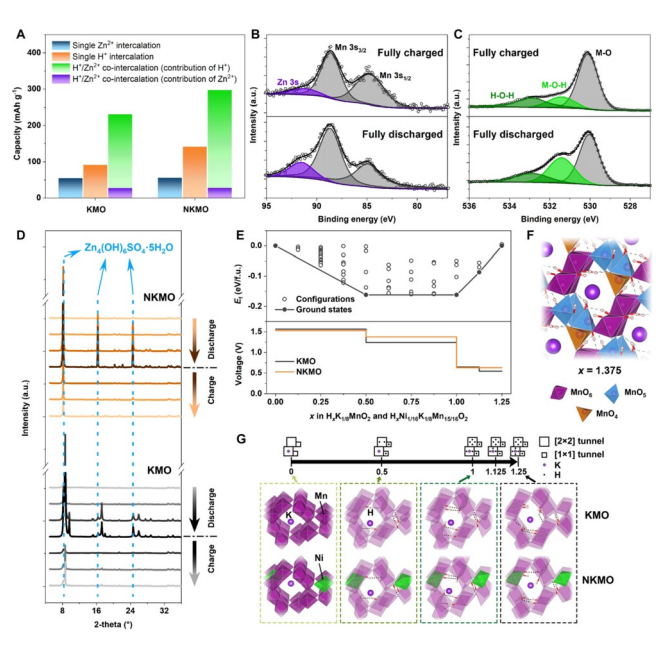


Figure 2. H<sup>+</sup>/Zn<sup>2+</sup> co-intercalation and the structural evolution during cycling. A) Capacities of KMO and NKMO electrodes using ZnSO<sub>4</sub>/ DMSO (single Zn<sup>2+</sup> intercalation), MnSO<sub>4</sub>/H<sub>2</sub>O (single H<sup>+</sup> intercalation) and  $ZnSO_4 + MnSO_4/H_2O$  (H<sup>+</sup>/Zn<sup>2+</sup> co-intercalation) electrolytes. For  $H^+/Zn^{2+}$  co-intercalation, the contributions of  $H^+$  and  $Zn^{2+}$  in electrode capacity are also indicated. B) and C) XPS spectra of (B) Mn 3s and (C) O 1s peaks for NKMO electrode at fully charged and discharged states. D) Ex situ XRD patterns at different states of charge for Zn/KMO and Zn/NKMO cells. E) The DFT-predicted formation energies,  $E_{fr}$  of all the H<sup>+</sup>-intercalation configurations (open circle) including the ground states in the convex hull (filled circle) for KMO, and the theoretical voltage profiles of both KMO and NKMO. F) Optimized structure of  $H_xNi_{1/16}K_{1/8}Mn_{15/16}O_2$  with x=1.375, in which some of the Mn ions will be displaced from the octahedral sites. G) Sequence of ground-state configurations through which H<sup>+</sup> ions are intercalated into KMO and NKMO.

and C. Since KMO and NKMO produce similar XPS patterns (Figure S12), here we emphasize on the results of NKMO. It can be seen that the intensity of Zn (at  $\approx$  91.3 eV) and M-O-H (at 531.4 eV)<sup>[12,17]</sup> peaks increases gradually upon discharge, and then decreases during recharging process (Figure S13 and S14), thus justifying the co-intercalation of  $Zn^{2+}$  and  $H^+$ . We note that whenever a H<sup>+</sup> is intercalated into the cathode, an OH would be left in the electrolyte, which, when accumulated to a certain level, will eventually lead to the formation of  $Zn_4(OH)_6(SO_4)\cdot 5H_2O$  (ZOSH) on the cathode surface.<sup>[18]</sup> The ZOSH products are removed before XPS tests by immersing in a dilute sulfuric acid. Figure 2D and S15 show the XRD patterns and SEM morphologies of KMO and NKMO electrodes without ZOSH removal at different charge/discharge states. The intensity of ZOSH peaks grows sharply for NKMO during the discharge period, which is much more prominent than that of KMO. This substantiates the above observation that Ni doping promotes H<sup>+</sup> intercalation. On the other hand, STEM energy dispersive spectroscopy (EDS) mapping of the electrodes (without ZOSH) verifies the successful intercalation of Zn2+ into the bulk phase of KMO and NKMO (Figure S16 and S17).

To shed light on the underlying relationship between Ni doping and the promoted H<sup>+</sup> intercalation, DFT calculations on the structural evolution during charge/discharge are conducted. In pristine α-MnO<sub>2</sub>, four symmetrically equivalent  $H^+$  intercalation sites exist in each cavity along the  $[2 \times 2]$ tunnel, while in the  $[1 \times 1]$  tunnel each cavity can only be occupied by one H<sup>+</sup> ion (Figure S18). The computed formation energies of different intercalation configurations for  $H_xK_{1/8}MnO_2$  and  $H_xNi_{1/16}K_{1/8}Mn_{15/16}O_2$ , corresponding to KMO and NKMO, are shown in Figure 2E. Here, the upper bound of H<sup>+</sup> intercalation is determined to be x = 1.25, above which significant distortion of MnO<sub>6</sub> structural units will occur, with some of the Mn ions migrating to nearby tetrahedral sites (Figure 2F). From the derived convex hull, we obtain the theoretical voltage profiles for KMO and NKMO. Two predicted discharge plateaus (vs. Zn/Zn<sup>2+</sup>) at 1.56 (1.53) and 1.24 (1.38) V for KMO (NKMO) indicate the good agreement between theoretical and experimental results. Voltage drops to below 1 V at x = 1, meaning that for both electrodes, the theoretical discharge capacity above 1 V is 1 H per formula unit. Therefore, the capacity limit remains unchanged upon Ni doping, and the experimentally observed increase in H<sup>+</sup> intercalation capacity upon Ni doping could not be ascribed to thermodynamic origins. Figure 2G shows the structural transformation of both electrodes upon H<sup>+</sup> insertion, in which the tetragonal-orthorhombic (TO) distortion of the lattice is observed, accompanying with the establishment of hydrogen bonds inside both  $[2 \times 2]$  and  $[1 \times$ 1] tunnels. Previous studies on Li intercalated α-MnO<sub>2</sub> have reported this kind of distortion and proposed that such changes could be attributed to Jahn-Teller deformation of [Mn<sup>3+</sup>O<sub>6</sub>] octahedrons.<sup>[19]</sup> The TO distortion offers an additional basis for rationalizing the essential role of Ni dopants, which will be focused on in the following discussion.

The degree of TO distortion can be quantified by both the interlayer spacing of (200) planes and the joint angle ( $\theta$ ) between corner-shared MnO<sub>6</sub> blocks, as depicted in Fig-

. 8, Downloaded from https://onlinelibrary.wiley.com/doi/10.1002/anie.202011588 by University Town Of Shenzhen, Wiley Online Library on [24/11/2025]. See the Terms and Conditions (https://onlinelibrary.wiley.com/rerms-and-conditions) on Wiley Online Library for rules of use; OA articles are governed by the applicable Creative Commons. License

5213773, 2021, 8, Downloaded from https://onlinelibrary.wiley.com/doi/10.1002/anie.202011588 by University Town Of Shenzhen, Wiley Online Library on [24/11/2025]. See the Terms and Conditions (https://onlinelbrary.wiley.com/terms-and-conditions) on Wiley Online Library of rules of use; OA articles are governed by the applicable Creative Commons. Licensea

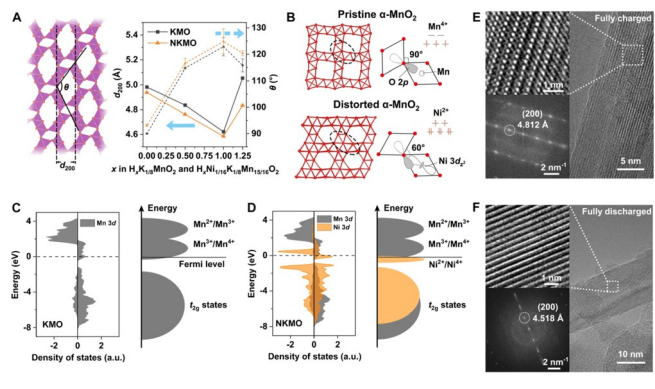


**Figure 3.** Effects of Ni-doping on tetragonal-orthorhombic distortion. A) The predicted interlayer spacing of (200) planes,  $d_{200}$ , and the joint angle between corner-shared MnO<sub>6</sub> blocks,  $\theta$ , as a function of H<sup>+</sup> content. B) Oxygen framework in pristine and distorted α-MnO<sub>2</sub>, and schematics of the interaction between O 2p and transition metal 3d states. (C and D) DOS of the Mn and Ni 3d orbitals in C) KMO and D) NKMO, and the schematics of the corresponding band structures. Fermi level is set to zero. E and F) STEM analysis and corresponding SAED patterns of (E) fully charged and (F) fully discharged states of NKMO electrode.

ure 3 A. In both KMO and NKMO, the (200) interlayer distance is contracted by  $\approx 7\,\%$  from x=0 to x=1. Differential elongation of the Mn–O bonds upon discharge is found (Figure S19), implying that Mn<sup>4+/3+</sup>O<sub>6</sub> octahedra undergo concerted deformation to relieve the internal stress induced by TO distortion. The O ions at the middle of the walls of the [2 × 2] tunnel become closer to each other with increasing degree of distortion (Figure 3 B), thereby facilitating the formation of hydrogen bonds. We note that Ni doping gives rise to smaller  $d_{200}$  and larger  $\theta$ , that is, more significant TO distortion

A key factor in the doping effects is probably the electronic structure of Ni ions, which can be described by the electronic density of states (DOS) shown in Figure 3 C and D. For KMO, the donated electrons from pre-intercalated K transfer to the bottom of conduction band, which is constituted by the Mn 3d states. Mn is reduced with its average valence state below 4+. In NKMO, Ni dopant generates defect states near the conduction band minimum of α-MnO<sub>2</sub> and shows a propensity to accept the 4s electrons from K (the charge density is shown in Figure S20). With an atomic ratio of 2:1 between K and Ni ions, each Ni ion would receive 2 electrons, leading to a reduction from  $Ni^{4+}$  to  $Ni^{2+}$  and a slight increase of Mn valence state. It is worth mentioning that the XPS results (Figure S12) indicate a decrease in the energy splitting of Mn 3s doublet peaks upon Ni doping (from 4.979 eV for KMO to 4.817 eV for NKMO), corroborating with our theoretical prediction of the increased valency of Mn ions. From the DFT calculations, we find that the valence state of Ni ions in NKMO remains nearly unchanged during discharge (Table S2), implying that Ni have no direct contribution to the redox reaction of the electrode. This is consistent with the theoretical finding that Ni doping does not alter the capacity limit of  $\alpha$ -MnO<sub>2</sub>.

According to the crystal field theory, Mn<sup>4+</sup> ion in octahedral coordination exhibits an orbital occupation of

 $t_{2g}^3 e_{\rm g}^0$ , while Ni<sup>2+</sup> ion has  $t_{2g}^6 e_{\rm g}^2$  configuration (Figure 3B). The low-lying  $t_{2g}$  orbitals  $(d_{xy}, d_{yz})$  and  $d_{xz}$  will not participate in bond formation between transition metal and O ions, whereas the high-lying  $e_g$  orbitals  $(d_{x^2-y^2}, d_{z^2})$  are antibonding. Therefore, increasing the electrons in  $e_{\sigma}$  orbitals, as occurs in  $H_{\kappa}K_{1/2}$  $_{8}$ MnO<sub>2</sub> (x > 0) intermediates and by substituting Mn<sup>4+</sup> with Ni<sup>2+</sup>, which provides even stronger metal-oxygen interactions due to two occupied  $e_g$  electrons on Ni<sup>2+</sup>, will result in destabilization of the tetragonal lattice. In the distorted Nidoped  $\alpha$ -MnO<sub>2</sub>, the occupied d<sub>z<sup>2</sup></sub> orbital of the transition metal ion has relatively weaker spatial overlap with the O 2p orbital as compared with the case in pristine α-MnO<sub>2</sub>, where the O 2p orbital tends to polarize its electrons toward the octahedral sites. Our analysis implies that the TO distortion exerted by Ni dopants can be rationalized by the tendency to lower the orbital energy of the antibonding states. The variation in distortion can also be confirmed by HRTEM and the corresponding selected area electron diffraction (SAED) results in Figure 3 E,F, and S21, in which the interlayer spacing of (200) plane (4.518 Å at discharged state) of NKMO electrode is relatively smaller than that of KMO (4.571 Å at discharged state).

To provide a mechanistic account of how  $H^+$  ions diffuse in the tunnels and how Ni dopants influences  $H^+$  intercalation, we perform climbing-image nudged elastic band calculations that consider different  $H^+$  hopping schemes in the [2 × 2] tunnel. When there is no lattice distortion (Figure 4A), direct hopping of  $H^+$  ion involves a transition state where the  $H^+$  is bonded to two neighboring O ions. The activation energy is as high as 1.28 eV (Figure 4C), indicating extremely sluggish diffusion of  $H^+$  ions in the tunnel. In comparison,  $H^+$  diffusion barrier in the [1 × 1] tunnel is 0.83 eV (Figure S22). When the TO distortion is imposed (Figure 4B), hydrogen bonds are established and a new  $H^+$  diffusion pathway appears, which bears remarkable resemblance to the Grot-

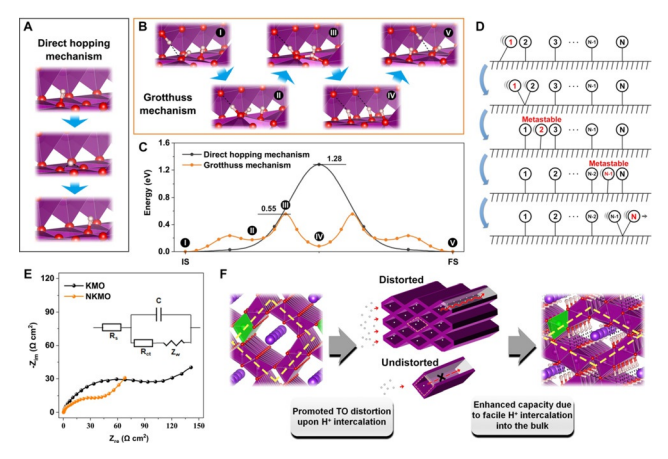


Figure 4. The kinetics of protons in distorted α-MnO<sub>2</sub>. A) H<sup>+</sup> ion migration pathway via direct hopping along the [2×2] tunnel in α-MnO<sub>2</sub>. B) Grotthuss proton transport of three H<sup>+</sup> ions along the [2×2] tunnel in distorted α-MnO<sub>2</sub>. C) The corresponding energy barriers for both H<sup>+</sup> migration mechanisms. D) Schematic illustration of Grotthuss mechanism for cooperative diffusion of a H<sup>+</sup> array. E) EIS spectra of KMO and NKMO electrodes at potential 1.39 V vs. Zn/Zn<sup>2+</sup>. F) Proposed mechanistic model of how TO distortion regulates the capacity of  $\alpha$ -MnO<sub>2</sub>.

thuss proton hopping in water. Along this pathway, the O ion on the wall of the  $[2 \times 2]$  tunnel accepts two H<sup>+</sup> ions (Configuration II) after the facile transfer of H<sup>+</sup> via hydrogen bonds (I  $\rightarrow$  II). The transition state (Configuration III) during subsequent H<sup>+</sup> transfer process (II  $\rightarrow$  IV) is overcome by the energy gain due to the transformation from the weakly-bound -OH<sub>2</sub> to stable -OH configuration. In Configuration IV, the H<sup>+</sup> is situated at a metastable site, that is, on an O ion that lies at the corner of the  $[2 \times 2]$  tunnel. Such a scenario is made possible by the TO distortion that stabilizes this metastable structure. The processes  $IV \to V$  and  $IV \to I$  are identical and hence display the same energy landscape. As a consequence, the energy barrier of this mechanism (0.55 eV) is significantly lower than that of direct hopping mechanism. Figure 4D and S23 visualizes the Grotthuss mechanism for cooperative diffusion of a long H+ array. It can be concluded that Grotthuss proton transport is critical for fast H<sup>+</sup> intercalation into α-MnO<sub>2</sub>, and the Ni dopants, which promotes TO distortion, can accelerate the  $H^+$  diffusion in the  $[2 \times 2]$ tunnels by advancing the onset of Grotthuss hopping Scheme.

The electrochemical reaction kinetics is further evaluated by electrochemical impedance spectroscopy (EIS). The results of KMO and NKMO in Figure 4E show semicircles associated with interfacial resistance and a diffusion tail corresponding to  $H^+/Zn^{2+}$  co-intercalation.<sup>[20]</sup> The NKMO electrode presents steeper diffusion slope and smaller semicircle value than KMO, indicating the efficiency of Ni doping on boosting the kinetics of H<sup>+</sup>/Zn<sup>2+</sup> ions. In addition, the relationship between the peak current (i) and the scanning rate (v) in CV curves can be described as  $i = av^b$ , where a larger value for b signifies more facile diffusion of the charge carriers.<sup>[21]</sup> For NKMO (Figure S24), the b values of all peaks (0.695-0.846) are higher than that of KMO (0.646-0.707), which justifies the theoretical analysis above. The diffusion coefficients of KMO and NKMO calculated on the basis of CV curves (Table S3) suggest a lower hindrance to diffusion upon H<sup>+</sup> extraction than H<sup>+</sup> intercalation, consistent with the expectation that Grotthuss mechanism is prominent with high H<sup>+</sup> concentration while the direct hopping mechanism prevails at dilute H<sup>+</sup> limit.

A summary of the proposed causal link between Ni doping and the improved energy density of  $\alpha$ -MnO<sub>2</sub> electrode is shown in Figure 4F. According to experimental measurements and DFT calculations, the possibility that Ni dopants introduce extra intercalation sites for H<sup>+</sup> is excluded since the dopants are not redox-active in NKMO. Instead, more serious TO distortion is accumulated in the presence of Ni, which can mediate the cooperative motion of H<sup>+</sup> ions. Also facilitated by TO distortion is the formation of hydrogen bonds, which initiates the Grotthuss hopping Scheme. This diffusion mechanism dramatically improves the kinetics of H<sup>+</sup> as compared with direct hopping mode and permits rapid ion access to the redox-active sites in the bulk of α-MnO<sub>2</sub>. At low levels of H<sup>+</sup> intercalation, the H<sup>+</sup> in pristine α-MnO<sub>2</sub> would be easily trapped in the  $[2 \times 2]$  tunnel if TO distortion is not successfully created, thus leaving empty intercalation sites in this tunnel after discharge. The higher propensity of TO distortion originating from Ni doping could circumvent the above issue, therefore exemplifying that the proton diffusion mechanism is tunable simply by compositional modification and can be optimized for obtaining a higher capacity. The derived conclusion that TO distortion exacerbated by Ni dopants enhances the capacity delivery of  $\alpha\text{-MnO}_2$ , can in turn be regarded as an excellent support to the proposed Grotthuss mechanism. Moreover, it is worth emphasizing that the enhancement in capacity delivery is achieved not at the cost of decreased voltage or hampered cyclability, which ensures a high energy density of the electrode during long-term cycling. We anticipate that the electrochemical performance of  $\alpha\text{-MnO}_2$  can be further improved by a combination of compositional tuning and nanostructure design, which entails further investigation in this area.

### Conclusion

In this work, we have demonstrated that Grotthuss proton transport plays a key role in the electrochemical performance of  $\alpha$ -MnO<sub>2</sub>, and can be modulated by compositional control, such as Ni doping. Upon discharge, large numbers of H<sup>+</sup> and a small ratio of  $Zn^{2+}$  ions co-intercalate into the bulk of  $\alpha\text{-}$ MnO<sub>2</sub>, which is accompanied by TO distortion of the lattice. The Ni dopants can enable a higher degree of TO distortion whereby the established hydrogen bonds and the flattened energy landscape helps to promote Grotthuss proton transport in the  $[2 \times 2]$  tunnels. As a result, the Ni-doped  $\alpha$ -MnO<sub>2</sub> exhibits drastic improvement in electrochemical performance, including high capacity delivery of 303 mAh g<sup>-1</sup> and impressive energy density of 421 Wh kg<sup>-1</sup>, as well as excellent power density. This study presents a strategy of substitution doping for taming the tunnel structure of MnO2 and regulating the proton transport inside, which may allow for development of a wide variety of high-energy-density cathode materials for rechargeable aqueous batteries.

## **Acknowledgements**

This work is financially supported by National Key R&D Program of China (2016YFB0700600), Basic and Applied Basic Research Foundation of Guangdong Province (No. 2019A1515110094).

# **Conflict of interest**

The authors declare no conflict of interest.

**Keywords:** aqueous batteries  $\cdot$  manganese oxides  $\cdot$  metal-doping  $\cdot$  proton-storage

a) L. Yang, K. Yang, J. Zheng, K. Xu, K. Amine, F. Pan, Chem. Soc. Rev. 2020, 49, 4667 – 4680; b) J. Zheng, Y. Ye, F. Pan, Natl. Sci. Rev. 2020, 7, 242 – 245; c) J. Zheng, Y. Ye, T. Liu, Y. Xiao, C. Wang, F. Wang, F. Pan, Acc. Chem. Res. 2019, 52, 2201 – 2209; d) G. Qian, X. Liao, Y. Zhu, F. Pan, X. Chen, Y. Yang, ACS Energy Lett. 2019, 4, 690 – 701; e) Z. Zhuo, F. Pan, W. Yang, Chinese J. Struct. Chem. 2019, 38, 2009 – 2014.

5213773, 2021, 8, Downloaded from https://onlinelibrary.wiley.com/doi/10.1002/anie.202011588 by University Town Of Shenzhen, Wiley Online Library on [24/11/2025]. See the Terms and Conditions (https://onlinelbrary.wiley.com/terms-and-conditions) on Wiley Online Library of rules of use; OA articles are governed by the applicable Creative Commons. Licensea



- [2] a) X. Li, W. Ying, J. Wu, L. Yuan, Y. Huang, Chinese J. Struct. Chem. 2019, 38, 1999 2004; b) Y. Li, J. Zhou, S. Guo, Chinese J. Struct. Chem. 2019, 38, 1993 1998; c) Z. Zheng, M. Weng, L. Yang, Z. Hu, Z. Chen, F. Pan, Chinese J. Struct. Chem. 2019, 38, 2020 2026; d) J. Xiang, L. Yang, L. Yuan, K. Yuan, Y. Zhang, Y. Huang, J. Lin, F. Pan, Y. Huang, Y. Huang, Joule 2019, 3, 2334 2363; e) J. Hu, J. Zhang, Chinese J. Struct. Chem. 2019, 38, 2005 2008
- [3] a) G. Fang, J. Zhou, A. Pan, S. Liang, ACS Energy Lett. 2018, 3, 2480–2501; b) X. Zeng, J. Hao, Z. Wang, J. Mao, Z. Guo, Energy Storage Mater. 2019, 20, 410–437; c) H. Jia, Z. Wang, B. Tawiah, Y. Wang, C.-Y. Chan, B. Fei, F. Pan, Nano Energy 2020, 70, 104523; d) R. Qin, Y. Wang, Q. Zhao, K. Yang, F. Pan, Chinese J. Struct. Chem. 2020, 39, 605–614; e) D. Chao, W. Zhou, F. Xie, C. Ye, H. Li, M. Jaroniec, S.-Z. Qiao, Sci. Adv. 2020, 6, eaba4098; f) B. Dunn, H. Kamath, J.-M. Tarascon, Science 2011, 334, 928–935.
- [4] a) Q. Zhao, S. Ding, A. Song, R. Qin, F. Pan, Chinese J. Struct. Chem. 2020, 39, 388-394; b) W. Li, C. Han, Y. Wang, H. Liu, Chinese J. Struct. Chem. 2020, 39, 31-35; c) M. Liu, Q. Zhao, H. Liu, J. Yang, X. Chen, L. Yang, Y. Cui, W. Huang, W. Zhao, A. Song, Y. Wang, S. Ding, Y. Song, G. Qian, H. Chen, F. Pan, Nano Energy 2019, 64, 103942; d) M. Liu, L. Yang, H. Liu, A. Amine, Q. Zhao, Y. Song, J. Yang, K. Wang, F. Pan, ACS Appl. Mater. Interfaces 2019, 11, 32046-32051; e) C. Xu, B. Li, H. Du, F. Kang, Angew. Chem. Int. Ed. 2012, 51, 933-935; Angew. Chem. 2012, 124, 957-959.
- [5] a) Q. Yang, F. Mo, Z. Liu, L. Ma, X. Li, D. Fang, S. Chen, S. Zhang, C. Zhi, Adv. Mater. 2019, 31, 1901521; b) J. Zheng, G. Tan, P. Shan, T. Liu, J. Hu, Y. Feng, L. Yang, M. Zhang, Z. Chen, Y. Lin, J. Lu, J. C. Neuefeind, Y. Ren, K. Amine, L.-W. Wang, K. Xu, F. Pan, Chem 2018, 4, 2872 2882; c) Y. Yamada, J. Wang, S. Ko, E. Watanabe, A. Yamada, Nat. Energy 2019, 4, 269 280.
- [6] a) J. Xie, Z. Liang, Y.-C. Lu, Nat. Mater. 2020, 19, 1006; b) W. Xu, K. Zhao, W. Huo, Y. Wang, G. Yao, X. Gu, H. Cheng, L. Mai, C. Hu, X. Wang, Nano Energy 2019, 62, 275–281; c) Y. Yamada, K. Usui, K. Sodeyama, S. Ko, Y. Tateyama, A. Yamada, Nat. Energy 2016, 1, 16129.
- [7] W. Sun, F. Wang, S. Hou, C. Yang, X. Fan, Z. Ma, T. Gao, F. Han, R. Hu, M. Zhu, C. Wang, J. Am. Chem. Soc. 2017, 139, 9775– 9778.
- [8] a) H. Pan, Y. Shao, P. Yan, Y. Cheng, K. S. Han, Z. Nie, C. Wang, J. Yang, X. Li, P. Bhattacharya, K. T. Mueller, J. Liu, Nat. Energy

- **2016**, *1*, 16039; b) X. Gao, H. Wu, W. Li, Y. Tian, Y. Zhang, H. Wu, L. Yang, G. Zou, H. Hou, X. Ji, *Small* **2020**, *16*, 1905842.
- [9] Q. Zhao, X. Chen, Z. Wang, L. Yang, R. Qin, J. Yang, Y. Song, S. Ding, M. Weng, W. Huang, J. Liu, W. Zhao, G. Qian, K. Yang, Y. Cui, H. Chen, F. Pan, Small 2019, 15, 1904545.
- [10] a) Y. Jin, L. Zou, L. Liu, M. H. Engelhard, R. L. Patel, Z. Nie, K. S. Han, Y. Shao, C. Wang, J. Zhu, H. Pan, J. Liu, Adv. Mater. 2019, 31, 1900567; b) J. Huang, Z. Wang, M. Hou, X. Dong, Y. Liu, Y. Wang, Y. Xia, Nat. Commun. 2018, 9, 1–8.
- [11] Y. Yuan, C. Zhan, K. He, H. Chen, W. Yao, S. Sharifi-Asl, B. Song, Z. Yang, A. Nie, X. Luo, H. Wang, S. M. Wood, K. Amine, M. S. Islam, J. Lu, R. Shahbazian-Yassar, *Nat. Commun.* 2016, 7, 13374
- [12] N. Zhang, F. Cheng, J. Liu, L. Wang, X. Long, X. Liu, F. Li, J. Chen, Nat. Commun. 2017, 8, 405.
- [13] X. Wu, J. J. Hong, W. Shin, L. Ma, T. Liu, X. Bi, Y. Yuan, Y. Qi, T. W. Surta, W. Huang, J. Neuefeind, T. Wu, P. A. Greaney, J. Lu, X. Ji, Nat. Energy 2019, 4, 123-130.
- [14] K. Xu, Nat. Energy 2019, 4, 93-94.
- [15] G. Fang, C. Zhu, M. Chen, J. Zhou, B. Tang, X. Cao, X. Zheng, A. Pan, S. Liang, Adv. Funct. Mater. 2019, 29, 1808375.
- [16] a) J. Huang, X. Tang, K. Liu, G. Fang, Z. He, Z. Li, *Mater. Today Energy* **2020**, *17*, 100475; b) Q. Zhao, A. Song, S. Ding, R. Qin, Y. Cui, S. Li, F. Pan, *Adv. Mater.* **2020**, *32*, 2002450.
- [17] X. Liu, J. Yi, K. Wu, Y. Jiang, Y. Liu, B. Zhao, W. Li, J. Zhang, Nanotechnology 2020, 31, 122001.
- [18] S. Zhao, B. Han, D. Zhang, Q. Huang, L. Xiao, L. Chen, D. G. Ivey, Y. Deng, W. Wei, J. Mater. Chem. A 2018, 6, 5733-5739.
- [19] C. Zhan, T. Wu, J. Lu, K. Amine, Energy Environ. Sci. 2018, 11, 243–257
- [20] a) K. Zhu, T. Wu, K. Huang, Adv. Energy Mater. 2019, 9, 1901968; b) M. Tian, C. Liu, J. Zheng, X. Jia, E. P. Jahrman, G. T. Seidler, D. Long, M. Atif, M. Alsalhi, G. Cao, Energy Storage Mater. 2020, 29, 9-16.
- [21] a) T. Wei, Q. Li, G. Yang, C. Wang, Adv. Energy Mater. 2019, 9, 1901480; b) Z. Li, S. Ganapathy, Y. Xu, Z. Zhou, M. Sarilar, M. Wagemaker, Adv. Energy Mater. 2019, 9, 1900237.

Manuscript received: August 28, 2020 Revised manuscript received: September 29, 2020 Accepted manuscript online: October 29, 2020 Version of record online: December 21, 2020